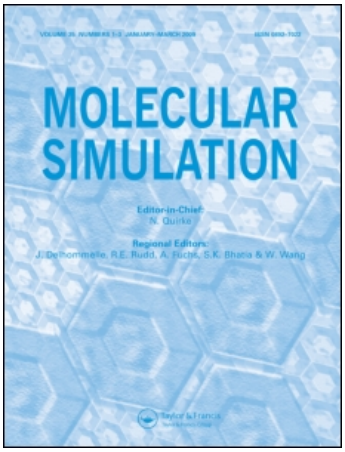

Molecular Simulation
Publication details, including instructions for authors and subscription information:
http://www.informaworld.com/smpp/title~content=t713644482

Interface Response Functions for Amorphous and Crystalline Si and the Implications for Explosive Crystallization

Erik J. Albenze[a]; Paulette Clancy[a]
[a] School of Chemical and Biomolecular Engineering, Cornell University, Ithaca, NY, USA

To cite this Article Albenze, Erik J. and Clancy, Paulette(2005) 'Interface Response Functions for Amorphous and Crystalline Si and the Implications for Explosive Crystallization', Molecular Simulation, 31: 1, 11 — 24
To link to this Article: DOI: 10.1080/08927020412331298658
URL: http://dx.doi.org/10.1080/08927020412331298658

Molecular Simulation, Vol. 31 (1), 15 January 2005, pp. 11–24

Interface Response Functions for Amorphous and Crystalline Si and the Implications for Explosive Crystallization

ERIK J. ALBENZE and PAULETTE CLANCY*

School of Chemical and Biomolecular Engineering, Cornell University, Ithaca, NY 14853, USA

(Received August 2004; In final form August 2004)

Interface response functions (IRFs) for amorphous and crystalline forms of Si have been determined for several empirical atomic-scale models using Molecular Dynamics and compared to available experimental results fitted to a Wilson-Frenkel equation form. Stillinger–Weber (SW), the environment-dependent intermolecular potential (EDIP), and a version of the modified embedded atom method (MEAM) models were found to produce unacceptable representations of the IRFs of both solid phases; they were either unable to predict the amorphous melting point and/or the maximum solidification velocity. The best of these models was judged to be the SW potential, known to produce a very accurate IRF for crystalline silicon. Increasing the strength of the three-body term by up to 25% above that of the original SW potential improves the prediction of the melting characteristics of the amorphous phase. Above this limit, liquid phase properties are impaired. The resultant IRFs provide an important backdrop to understand the kinetics of explosive crystallization (EC) processes, as we shall show in comparison to recent experimental data on the EC of amorphous Ge. [A. Chojnacka and M.O. Thompson, in *Growth, Evolution and Properties of Surfaces, Thin Films and Self-Organized Structures*, edited by S.C. Moss, D.B. Poker, D. Ila, (Mat. Res. Soc. Symp. Proc. 648, Warrendale, PA 2001) p. P11.12.1–8]. We also provide evidence that homogeneous melting within the bulk of the amorphous material competes with heterogeneous melting at the planar amorphous/liquid interface.

Keywords: Intermolecular potential; SW potential; Explosive crystallization; Interface

Pacs Codes: 64.70.Dv; 68.08.De; 81.15.Lm; 81.05.Cy

INTRODUCTION

Silicon forms two distinct solid phases, one crystalline and one amorphous. The melting point of the crystalline phase is 1685K, while reported melting points for the amorphous phase vary around a value of 1450 ± 50K. The melting points of the two phases are thus separated by just over 200° [1,2]. In common with a wide variety of substances, from metals to insulators, silicon is capable of exhibiting a phenomenon known as explosive crystallization (EC) in which an amorphous phase (*a*-Si, say) is converted to crystalline material (*c*-Si, say) at high speed [1,3–12]. For Si and other elemental semiconductors such as Ge, it is generally accepted that this self-sustaining process is mediated by a thin liquid layer. Driving this reaction are differences in the melting temperatures and enthalpies of the two phases. Once an initial liquid layer has been created (e.g. by the action of a laser), crystallization occurs rapidly. In the case of silicon, atoms crystallizing at the crystal/liquid interface will release heat which is then thermally conducted through the liquid to the liquid/amorphous boundary. The subsequent melting of amorphous Si withdraws heat from the system, encouraging further crystallization, causing the process to autopropagate. This is essentially a chain reaction process and, as such, it self-selects the fastest direction in which to propagate (for silicon, this is the [100] direction). The overall speed of EC is dictated by the kinetics of liquid phase crystallization which are expressed in the so-called interface response function (IRF) linking the velocity of melting and solidification to the thermodynamic driving force of interfacial overheating and undercooling, respectively. Here the velocity of the moving solid/liquid interface will be defined to be positive for solidification and negative for melting, following convention.

*Corresponding author. E-mail: pqc1@cornell.edu

ISSN 0892-7022 print/ISSN 1029-0435 online © 2005 Taylor & Francis Ltd
DOI: 10.1080/08927020412331298658

Several approaches have attempted to determine the IRF for Si [10,13–15] including fitting the limited experimental data that is available (the maximum solidification velocity and melting point) to a theoretical model such as the Wilson-Frenkel equation form [10], and combining the Wilson-Frenkel form with heat-flow calculations and time-resolved experimental data [10]. Atomic-scale simulation is an attractive alternative for IRF determinations due to the difficulties of experimental measurements caused by the high temperatures involved and the high speed (12–15 m/s) of the recrystallization front. Simulations also provide very detailed visualization of the atomic-scale nature of the solid–liquid interface and easily allow mechanistic and microscopic property determination (such as radial distribution function and local order).

To date, there has been one investigation of the IRF for amorphous Si [16], using both the EDIP and SW potentials. However, Ref. [16] reports the melting point of the SW-modeled amorphous phase to be 1450K, which is inconsistent with the results of Refs. [17,18,19], as well as our own studies presented here, all of which predict the melting point to be about 400K lower. IRFs to describe the kinetics of growth of crystalline Si are available for the EDIP [20] and SW crystals [21,22]. The results for the EDIP potential (the only potential with published results for both solid phases) suggest that this model is unable to accurately represent the melting points of both amorphous and crystalline phases of Si with a single parameterization (predicted melting points for crystal and amorphous phases are 1520 and 1200K, respectively). Yet this characteristic will be essential for our interest in accurately simulating EC processes which demands a model capable of representing the delicate heat balance involving the amorphous, liquid, and crystal phases in nanoscale proximity moving at high speed. No study has yet attempted to optimize a potential model so that it accurately determines the IRF for both amorphous and crystal silicon and this is the focus of the current paper. To that end, we will determine the IRFs of the original parameterization of the SW, EDIP and modified embedded atom method (MEAM) models for Si in both the crystalline and amorphous phases.

Given the failure of all these models to accurately represent the IRFs of *a*-Si and *c*-Si, as will be described in section "Results", IRFs were determined for reparameterizations of the SW potential seeking a model that fits our design criterion above. Given the best model yielded by this study, we are then able to discuss the implications for simulations of EC of Si (section "Implications for Explosive Crystallization"). Observation of the melting mechanism of amorphous Si showed that it warranted special consideration, explored in the section "Mechanism for Melting Amorphous Si".

INTERATOMIC POTENTIAL MODELS

The main aim of this study was to find (or develop, if necessary) a potential which does an acceptable job representing all three condensed phases of silicon (*a*-Si, *c*-Si and the liquid, *l*-Si). This goal poses a severe challenge for any potential, especially the empirical models considered here. The three potentials we tested were the commonly used Stillinger–Weber potential [23], the more recently developed EDIP potential [24–26], and a fit of the MEAM potential performed by Lenosky *et al.* [27,28].

The Stillinger–Weber potential was designed to predict the crystal-liquid melting transformation of Si. Thus, not surprisingly, it gives a good description of the liquid phase and the energetics of the crystal. It has a simple form consisting of a two- and three-body term with the three-body term written as follows:

$$\nu_3(r_i,r_j,r_k)=\varepsilon[h(r_{ij},r_{ik},\theta_{jik})+h(r_{ji},r_{jk},\theta_{ijk})+h(r_{ki},r_{kj},\theta_{ikj})]$$

$$h(r_{ij},r_{ik},\theta_{jik})=\lambda\exp\left[\gamma\left(\frac{r_{ij}}{\sigma}-a\right)^{-1}+\gamma\left(\frac{r_{ik}}{\sigma}-a\right)^{-1}\right]\times\left(\cos\theta_{jik}+\frac{1}{3}\right)^2 \quad (1)$$

where r_{ij} is the inter-atomic distance between atoms i and j, a is the potential cutoff, θ_{jik} is the bond angle for atoms i, j, and k, and the remaining variables are adjustable parameters.

This potential was developed to model the crystal and liquid phases, but no attention was paid to the nature of its amorphous phase. Investigations have shown that it has difficulty forming *a*-Si from the melt [17–19,29], though it can produce a credible amorphous silicon structure when *ad hoc* methods are used to prepare the sample, including applying negative pressure to a quenched liquid [19,29] or using a "bond-switching" method like the continuous random network [30] and then evolving this with the SW potential. Unfortunately, the coordination number of these *a*-Si samples is over 4.1, which compares unfavorably with the experimental value of 3.9. The melting point for SW-modeled amorphous silicon has been determined to be ~1050K [17–19], about 25% too low compared to experiment.

The EDIP potential is a recent adaptation of the SW potential in which the three-body portion contains an additional term, and both the two- and three-body terms contain dependence on the local coordination of the atom. Unlike the SW potential, which somewhat too aggressively encourages tetrahedral coordination for all phases, the EDIP potential contains so-called "environment dependence" which allows an atom to alter its bonding preference based on its nearest neighbors. This potential was

fitted to a database of *ab initio* data including the cohesive energy and lattice constant (for a diamond cubic structure), formation energies of some defects, selected self-diffusion and generalized stacking fault values, as well as experimental elastic constants. It readily forms a version of amorphous silicon directly from a liquid quench with structural properties in better agreement with experiment (a coordination number of 4.05) [26]. On the other hand, the melting point for the EDIP-modeled crystal phase has been reported to be anywhere from 1370K [26] to 1520K [20], about 20 and 10% too low compared to experiment (1685K). The reported melting temperature for the amorphous phase is 1200K [16] which is about 20% lower than experiment.

Lenosky *et al.* [27] used an extensive database of *ab initio* calculations including force and energy data, experimental elastic constants and phonon frequencies and energetics for vacancy and interstitial point defects to fit a form of the MEAM potential. The reported melting point for the crystal is only 1250K [27], about 25% too low. Nothing is known of the nature and characteristics of any amorphous phase that it might produce.

SIMULATION METHOD

Molecular Dynamics simulations were performed using a constant pressure–constant temperature ensemble with periodic boundary conditions in all three Cartesian directions using the leap-frog algorithm proposed by Brown and Clark [31]. The simulations consisted of "sandwich" configurations of solid and liquid phases, as shown in Fig. 1 for the solidification and melting of crystal Si. The sandwich samples were set up so that growth (or melting) would be in the [100] direction, since this is the direction which would be self-selected by EC. An analogous "sandwich" was constructed when considering amorphous Si and liquid phases. Two different amorphous silicon samples were used: One derived from a continuous random network sample [30], the other from a sample prepared by quenching a liquid (for SW see Ref. [19]). The sample preparation proved to be unimportant since both samples evolved from their differing starting points,

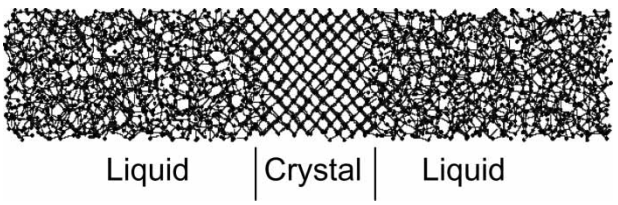

FIGURE 1 A typical "sandwich" configuration comprising of a crystalline phase placed between two liquid phases and used to determine the IRF for a crystal.

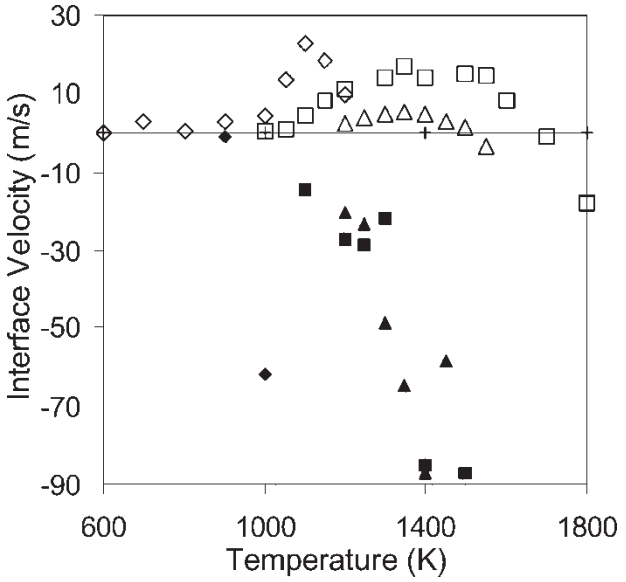

FIGURE 2 IRF for the original SW potential (*a*-Si: solid squares and solid line, *c*-Si: open squares), EDIP (*a*-Si: solid triangles and dotted line, *c*-Si: open triangles), and MEAM (*a*-Si: solid diamonds and dashed line, *c*-Si: open diamonds).

under the influence of their respective potentials, to a temporally unchanging configuration which was found to be structurally identical.

The systems ranged in size from 1536 to 16,384 atoms, with aspect ratios ranging from 3:1 to 12:1 depending on the sample size necessary to capture adequately the motion of the interface. Several runs of the largest samples (16,384 atoms, with an aspect ratio of 4:1) were performed for the EDIP, SW, and SW115 (described below) potentials but no sample size effects were found; results from the larger samples were coincident with those from the smaller samples on the scale of the data in Figs. 2 and 3. Indeed, the data points presented in Figs. 2 and 3 are an average of several data points (usually 2–6) for each temperature arising from anywhere from one to three different size samples (two data points for each size sample).

The samples were evolved at a pre-set undercooling to encourage solidification (or overheating for melting) and the motion of the solid–liquid interface was recorded by determining its location using appropriate order parameters. Here we used average bond angles, average bond angle deviations, and an angular order parameter, described below. The location of the interface was determined by dividing each sample into slices that were 1–2 atomic layers thick and deciding whether each slice was solid, liquid, or interfacial. The designation of each slice was determined by inspection of the previously mentioned order parameters. Once the location of the interface is known as a function of time it is straightforward to calculate the velocity of the planar interface by determining the distance

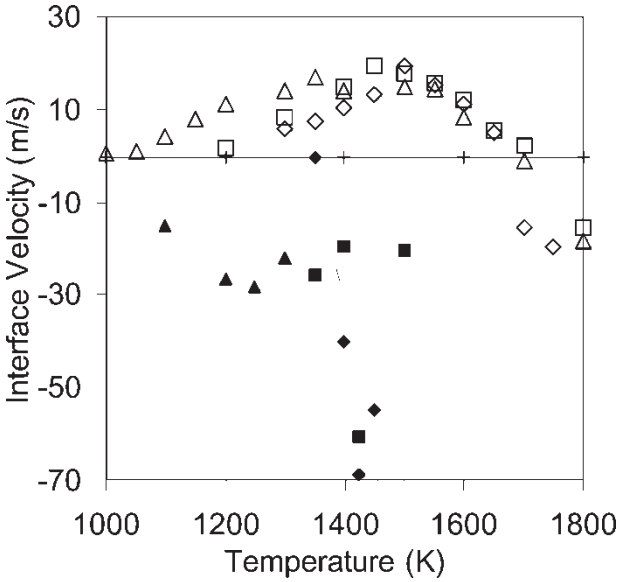

FIGURE 3 Comparison of the IRFs for SW125 (*a*-Si: solid diamonds and dotted line, *c*-Si: open diamonds) and SW115 (*a*-Si: solid squares and solid line, *c*-Si: open squares) with the original SW model (*a*-Si: solid triangles and dashed line, *c*-Si: open triangles).

moved over the time of the simulation. The melting point was determined to be the temperature at which the velocity of the interface was zero (ignoring the (0,0) point).

The angular order parameter [32] mentioned above designates an atom as being "solid-like" or "liquid-like". To be solid-like, an atom must have four nearest neighbors with the nearest neighbor cutoff being chosen as the first minimum in the radial distribution function and a value for $A < 0.4$ determined by the following equation:

$$A = \sum_i \left(\cos\theta_i + \frac{1}{3}\right)^2, \qquad (2)$$

where the sum is taken over the triplet sets of the four nearest neighbors and θ_i is the angle made by the triplet set (for the tetrahedral angle, $\cos\theta = -1/3$ so A will be equal to zero for perfect tetrahedral structure). If these criteria are not met, then the atom is designated liquid-like. Within each slice, the fraction of atoms considered to be solid was compared to characteristic values from "bulk"-like 512-atom samples for crystal (fraction of solid characteristically >99%) for liquid (0–45% solid-like), and for amorphous (60–90% solid-like)[†] to determine the nature of the slice. Interface determination for the liquid/crystal samples was uncomplicated since there was essentially a step change in the extant percentage of solid as a function of distance along the sample, clearly indicating the interface. Determination of the interface in the amorphous/liquid samples was more difficult and often subjective. The liquid and amorphous sections were regularly found to be separated by ambiguous slices (i.e. falling in the undefined 45–60% solid-fraction range). To address this problem, we chose the position of the interface to be the first unambiguously amorphous slice so that a consistent approach was taken in all cases. Average bond angles, and bond angle deviations, were used to help clarify the nature of ambiguous slices. We observed that, during the simulation, slices within the bulk of the *a*-Si section exhibited unexpectedly low order, to the extent of being classifiable as liquid-like. This observation was examined further, as described in section "Mechanism for Melting Amorphous Si."

RESULTS

Interface Response Functions for Existing Potential Models

Using the prescription described in the preceding section for determining the location and speed of a moving solid/liquid interface as a function of the temperature in the system, we were able to construct the IRF for each of the potential models described in section "Interatomic Potential Models" and for both crystalline and amorphous phases. The IRFs for the EDIP, SW and MEAM potential models are shown in Fig. 2. Our calculated IRFs are consistent with previously published data for both solid phases for the EDIP potential [16,20] and for the crystal phase of the SW potential [21,22] (within 5% for maximum velocities and melting points). As mentioned above, our results are not consistent with the published results of Ref. [16] for the SW-modeled amorphous phase due to a discrepancy in the melting point between their results and ours. The melting point we determined is, however, consistent with those in Refs. [17–19]. The differences between the results for the SW potential between the data in Ref. [16] and others could be due to the precise nature of the amorphous phase that they used for their investigations. Preparation of a sufficiently evolved amorphous sample is difficult to produce computationally [17–19,29] for the SW potential. There is insufficient detail on the preparation of the amorphous sample in Ref. [16] to allow us to make any further comments on this point.

Each of our calculated IRFs for the solidification of the crystal phase shows the expected form of

[†]The percentage of solid values in samples containing both liquid and amorphous bulk samples are somewhat temperature-dependent, resulting in the ranges of 60–90% for amorphous and 0–45% for liquid samples. The crystal phase shows some temperature dependence, but over a far smaller range (99–100%).

TABLE I Maximum crystal resolidification velocity and amorphous phase melting point for three empirical models of group IV materials

Model	$V_{max,\ cryst}$	$T_{m,\ amorph}$
SW	17	1075
EDIP	5.3	1175
MEAM	22.5	900
Experiment	15.8	1450

Experimental values come from Refs. [1,2,9–11,37].

the function, decaying to zero at both 0K and at a second point identified as the equilibrium melting point, and exhibiting a maximum in the growth curve. As can be seen in Fig. 2, the predictions of the maximum growth velocity and the melting points vary significantly (see Table I). It is also obvious that none of these models accurately predicts the melting points of both *a*-Si and *c*-Si and gives a reasonable maximum growth velocity for *c*-Si.

The melting points for the amorphous and crystal phases of the EDIP potential are too low, but have the merit of exhibiting close to the experimental difference between them (335K for EDIP vs. 230K experimentally), but the maximum crystal growth velocity is far too low (5.3 m/s). Examination of the EDIP model provides some insight into its sluggish behavior with respect to the crystal growth velocity. The model was developed on the premise that local order determines the type of bonding. Since atoms near the crystal–liquid interface possess a coordination number intermediate between the two phases, the EDIP model will adjust the energy to try to accommodate the perceived local order, thus not forcing tetrahedral order and crystalline growth. This could explain the overly slow solidification behavior observed. Unfortunately, this means that the EDIP model, however useful for bulk properties, is not well suited for our purposes.

The Lenosky *et al.* fit of the MEAM model has a good description of the maximum growth velocity of *c*-Si but the melting points of the solid phases are much too low (38 and 28% error for the amorphous and crystal melting points, respectively). As was already known, the SW potential has the most reasonable description of the IRF for *c*-Si, but its prediction of the melting point of the amorphous phase is about 25% too low, making the difference in melting points of the two solid phases much too large.

For the SW potential to be useful in the simulation of EC, the behavior of the amorphous phase needs to be improved. One obvious way to achieve this is to increase the three-body term in the potential; this has previously been shown to give better structural properties for amorphous silicon [17,33]. Vink *et al.* found *a*-Si structures comparable in quality to the CRN model if the three-body term in SW was increased by 50% [33]. The effect of this increase on the melting point of *a*-Si was not investigated. Since both the crystal and amorphous phases are tetrahedral, in terms of local order, increasing the three-body term should increase the melting point while decreasing the relative melting point gap. Tuning the ε (energy) parameter thus provides a means of fitting the melting points. The strength of the three-body term can be varied until both melting points (amorphous and crystalline) accurately represent the experimental data.

Results for Modified SW Potentials

We tested the effect of changing the three-body term to 0.8, 0.9, 1.15, 1.25 and 1.5 of its original strength. Not surprisingly, reducing the three-body potential (0.8 and 0.9) destabilized the solid structures. The samples corresponding to a 50% increase in the three-body term (like that suggested by Vink *et al.*) gave no volume change on melting and hence increases as large as 50% in the three-body term was dismissed as non-physical. Increasing the 3-body forces by 15% (henceforth referred to as SW115) and 25% (SW125) gave more promising results, including better structural properties for the amorphous phase as well as significantly better melting temperatures. Plots of the IRFs for these modified SW models are shown in Fig. 3; their structural properties are shown in Table II and thermodynamic properties in Table III.

TABLE II Structural properties for the modified SW potentials for liquid and amorphous phases as compared to experiment

Liquid	*Average bond length*	*Average bond angle*	*CN*	*AOP*
SW100	2.78 ± 0.29	98.7 ± 32.3	7.3	0.001
SW115	2.75 ± 0.31	99.8 ± 31.4	6.0	0.019
SW125	2.75 ± 0.31	100.0 ± 31.2	5.6	0.028
Experiment	–	–	6.4	–
Amorphous	*Bond length*	*Bond angle*	*CN*	*AOP*
SW100	2.41 ± 0.11	108.2 ± 14.5	4.13	0.824
SW115	2.41 ± 0.11	108.7 ± 12.6	4.05	0.889
SW125	2.41 ± 0.11	108.7 ± 12.4	4.04	0.897
Experiment	–	108.6 ± 10	3.9	–

Units are Å for the average bond length and degrees for the mean bond angle. Experimental values from Refs. [34,35]. The final two columns refer to coordination number and angular order parameter, respectively.

TABLE III Thermodynamic properties for the modified SW potentials in comparison to experiment

Model	*Crystal*		*Amorphous*	
	T_m/K	ΔH_m	T_m/K	ΔH_m
100%	1680	0.341	1075	0.068
115%	1700	0.313	1325	0.058
125%	1660	0.363	1350	0.053
Experiment[33]	1680	0.522	1450	0.354

Values for ΔH_m are given in eV/particle.

Radial distribution functions for the two models, as compared with the original SW model, are shown in Fig. 4.

The reparameterized fits offer some improvement over the original Stillinger–Weber potential with minimal negative effects on the reproduction of the IRF for the crystal. The melting point of the amorphous phase improved significantly, as expected (although they are still in error by 9 and 7% for the SW115 and SW125 potentials, respectively). The structural properties of the liquid also improved in the case of the SW115 potential, as demonstrated by a coordination number of 6.0 as compared to 7.3 for the original SW potential (experimental value for the coordination number is 6.4). The enthalpy values of the original SW model were already quite inaccurate and became slightly worse in the case of the amorphous phase for the SW115 potential (0.058 vs. 0.354 eV/atom experimentally [34]), the SW125 potential (0.053 vs. 0.354 eV/atom), and the crystal phase for the SW115 potential (0.313 vs. 0.522 eV/atom [34]). The properties of *a*-Si were significantly improved, particularly the coordination number (CN = 4.05 and 4.04 for SW115 and SW125 potentials) and bond angle deviations (ΔBA = 12.6° and 12.4° for the SW115 and SW125 potentials, respectively), both of which are now in reasonable agreement with experiment (CN = 3.9 and ΔBA = 9.4–11.0°) [35,36]. It is not surprising that the coordination number remains higher than the experimental value since a classical potential has yet to be found that can stabilize an amorphous sample with a coordination number less than 4. However, and quite importantly, the IRFs for the modified SW models maintain the maximum velocity of the original model. Further increasing the strength of the three-body term to 25% produces only modest improvement in the properties of *a*-Si at the expense of a more significant loss in quality of the characteristics of the liquid phase. For these reasons, we chose to use a SW model enhanced by 15% in its three-body term for the remainder of the results shown here; the parameters for this new fit are provided in Table IV. We contend that this new model represents an improvement over the original SW model when all three phases (*l*-, *c*- and *a*-Si) have to be considered, though it necessarily involves some compromises relative to fitting the SW parameters for a single phase.

With the choice of interatomic model set (SW115), further simulations were run using different ensembles and simulation set-ups, not only to produce more data, but also to eliminate any effect of simulation technique on the resultant IRF. Runs were performed using constant-pressure/constant-temperature (NPT) and constant-volume/constant-temperature (NVT) ensembles as described by Brown and Clarke [31] and employing the sandwich configuration of Fig. 1 as the starting point. A second set of NVT simulations was performed with

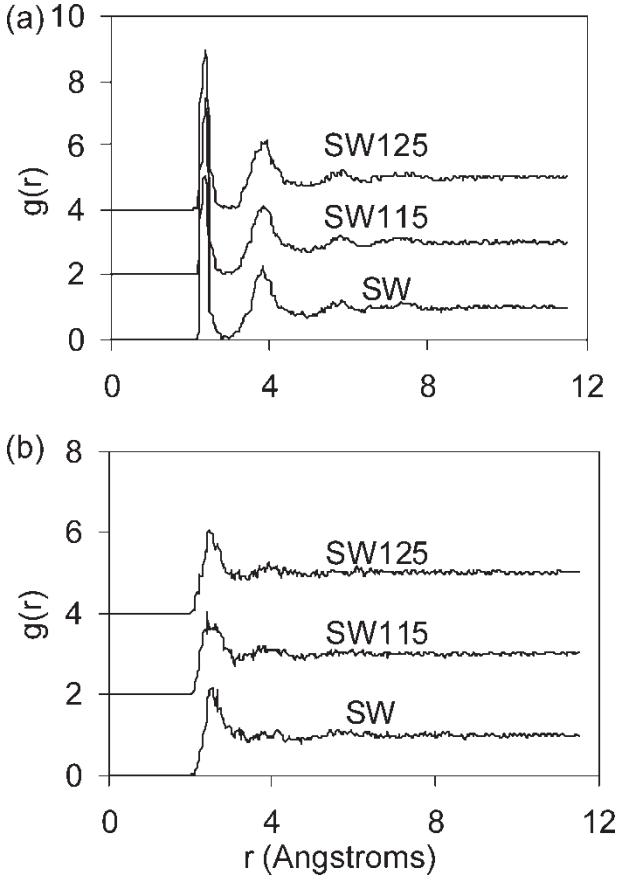

FIGURE 4 Comparison of radial distribution functions for all three SW potentials (SW125, SW115, and the original SW model shown as "SW") for the amorphous (a) and liquid phases (b).

TABLE IV Original and modified SW parameters

Parameter	*Original SW19*	*SW115*
λ	21.0	24.15
γ	1.20	1.20
A	7.049556277	7.049556277
B	0.602224558	0.602224558
A	1.80	1.80
P	4	4
Q	0	0
ε	50 kcal/mol	35 kcal/mol
σ	0.20951 nm	0.20951 nm

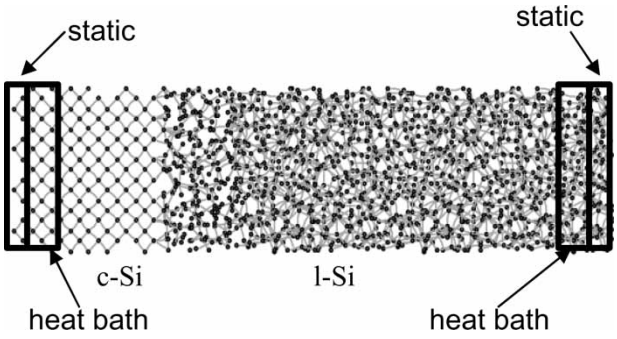

FIGURE 5 Starting sample configuration for constant-temperature simulations in which the temperature was maintained using heat baths abutting static boundaries.

temperature controlled by heat baths at the extreme edges of the simulation box, arranged as in Fig. 5. For these latter runs, periodic boundary conditions were used in the y- and z-directions only. The last four atomic layers on each end of the simulation cell were frozen to eliminate surface effects. For this new set of simulations, some runs (for all simulation techniques) were also performed to determine the freezing curve for amorphous silicon. We considered system sizes ranging from 3584 to 16,384 atoms with aspect ratios ranging from 4.0 to 12.0. As with the results above, no system size effects were noticed over the size range used for this study. The results for all of these simulations are presented in Fig. 6. A Wilson-Frenkel curve fit to the data is also presented.

A comparison of the prediction of the IRF using atomistic simulation results to those calculated using the few available experimental data fitted to the parameters of a continuum Wilson-Frenkel equation [10] is shown in Fig. 7. Though the shapes of both sets of curves are similar, quantitative differences are clearly seen, reflecting problems with both the effect of the compromised melting point of the amorphous phase for the atomistic simulations and the inherent inaccuracies of assumptions used in the Wilson-Frenkel fit. The largest discrepancy appears in the maximum solidification velocity of the amorphous phase, but this value is not well known experimentally. Experimental data [37] suggests that the value is at least 25 m/s which lies between the two computational values taken from Fig. 7.

IMPLICATIONS FOR EXPLOSIVE CRYSTALLIZATION

Our particular interest in determining the IRF of empirical models of Si lies in their importance as background information relevant to the simulation of EC. In this phenomenon, a crystal front advances at the expense of a liquid front and a second liquid front advances at the expense of the amorphous

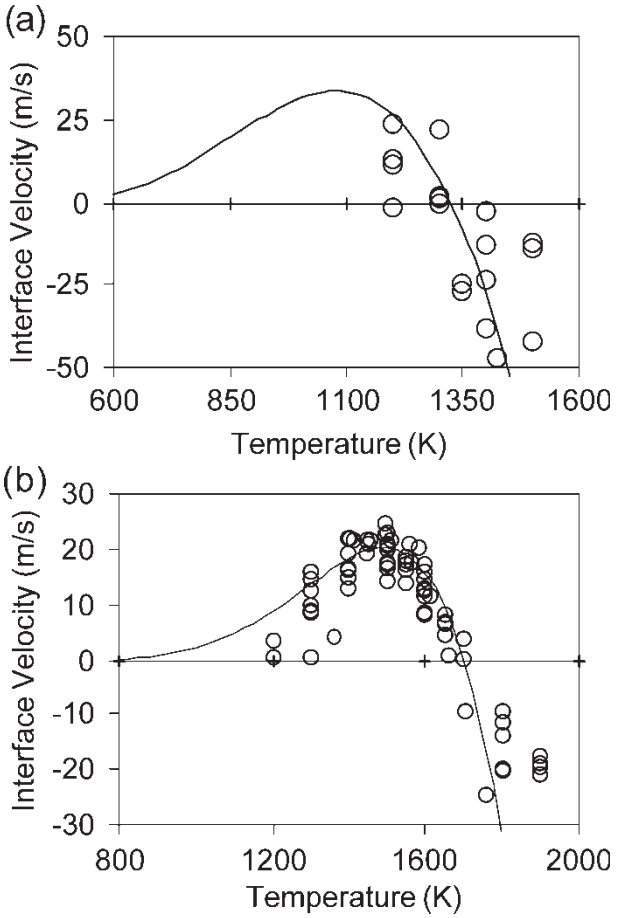

FIGURE 6 Interface response functions for (a) amorphous silicon and (b) crystalline silicon for the SW115 potential. Fits of the raw simulation data (shown as open circles) to a Wilson-Frenkel equation are shown as solid lines.

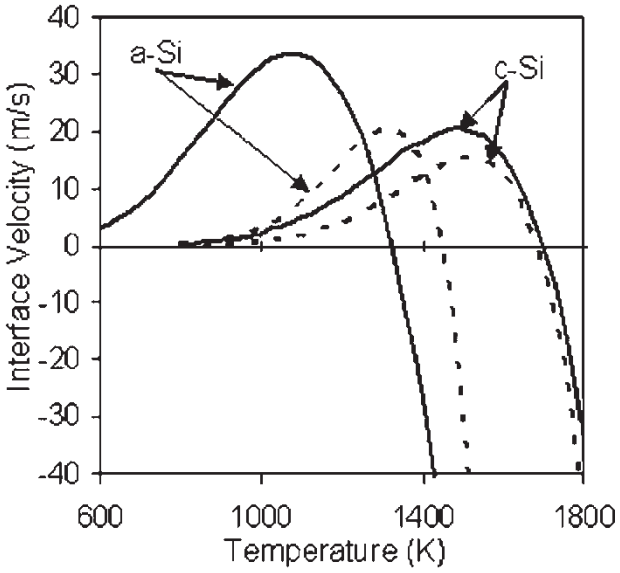

FIGURE 7 Comparison of results for the IRFs of amorphous and crystalline phases using the SW115 model (solid lines) with a modelling approach that combines experimental data within heat-flow calculations (dashed lines) [10].

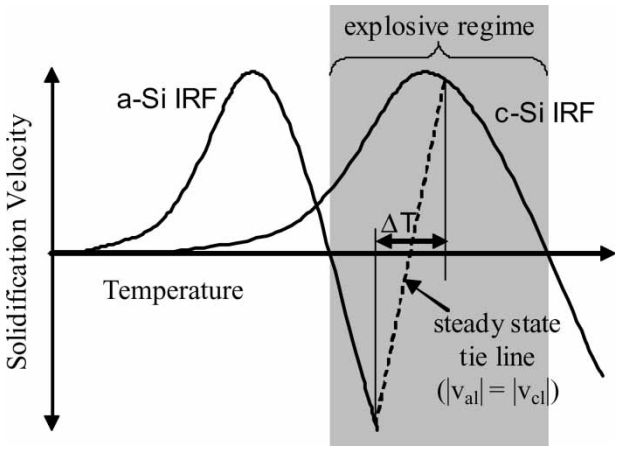

FIGURE 8 Connection between the explosive crystallization regime and the interface response functions of crystalline and amorphous materials.

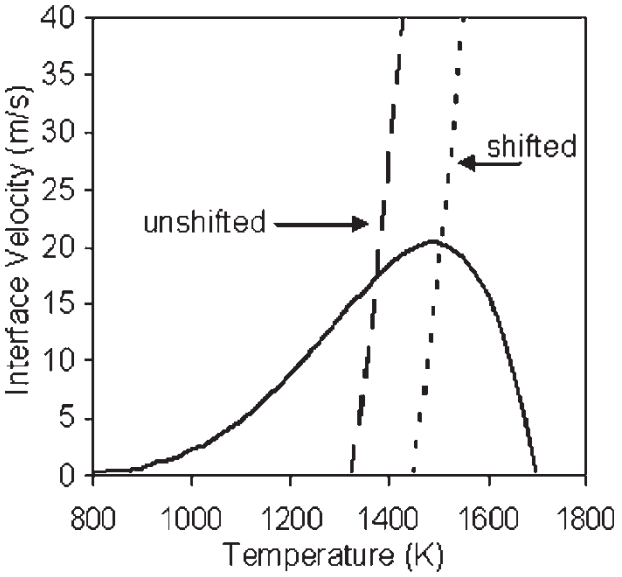

FIGURE 9 Wilson-Frenkel fits to the IRF data for SW115 silicon (*c*-Si: solid-line; locus of the modulus of the *a*-Si data determined from the raw simulation data: dashed line; same locus for the *a*-Si data shifted to reproduce the experimental melting point of *a*-Si: dotted line).

front, the two interfaces moving in response to their IRFs. At steady-state during EC, the liquid layer is believed to maintain a constant thickness, thus both interfaces must be moving at the same velocity. This allows us to predict the temperature difference across the liquid layer, as shown in Fig. 8. For example, EC in Si is known to occur at speeds near 15 m/s [1,9–11,38]; thus, by determining the temperature at which the fronts can move at this velocity, it is possible to get an estimate for the temperature difference across the liquid layer. Of course, this depends on the assumption that the mediating liquid layer in EC can really be considered as a "bulk"-like liquid. The nanoscale dimensions of the liquid layer implied by recent experiments [39] potentially challenges this assumption. However, computer simulations of solid–liquid interfaces suggest that bulk-like properties are re-established within 20 Å, suggesting that the assumption of bulk-like liquid properties will be reasonable even if the mediating liquid layer is only a few nanometers thick.

A plot of the IRF for the SW115 potential is presented in Fig. 9 showing only the growth portion for the crystal phase and the melting portion for the amorphous phase, plotted such that the *y*-axis represents the magnitude of the velocity. To account for the inaccurate melting point prediction, "shifted" data is also presented where the data is displaced along the *x*-axis (but maintaining its original slope) until it predicts the correct T_m. This is done with the justification that the melting portion of the amorphous IRF has consistently been found to be approximately linear, thus, shifting the data maintains the slope of the linear portion of the IRF while correcting for the inaccuracy in the melting temperature.

Figure 9 allows a prediction of the temperature difference across the liquid layer. For an EC velocity of 15 m/s, the predicted temperature difference is 170 and 45K for the unshifted and shifted data, respectively. Of course, the temperature difference values are determined using the fit to the scattered amorphous data and should be taken as a rough estimate. As expected, the incorrect prediction of the melting point makes it impossible to get anything more than an upper limit on the temperature difference across the liquid region.

Another phenomenon which can be determined by a study of the IRFs is whether EC occurs by so-called

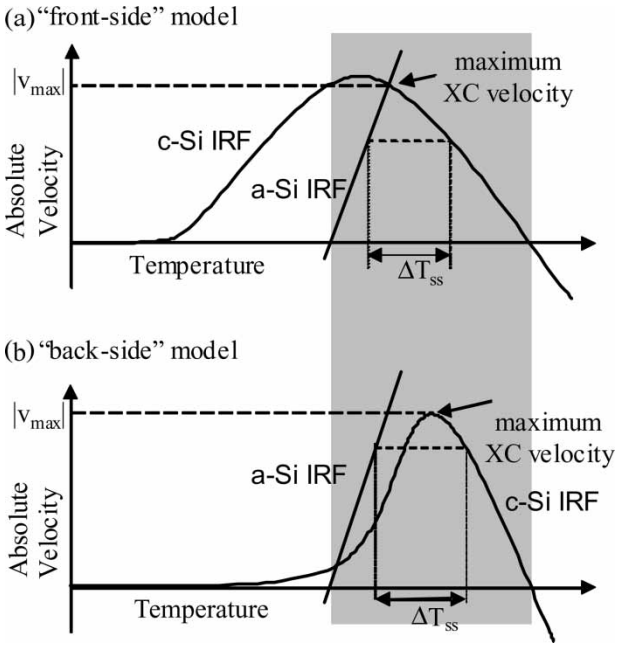

FIGURE 10 Schematic showing (a) front-side and (b) back-side models of explosive crystallization.

"back-side" or "front-side" growth, explained in Fig. 10; terms coined by Chojnacka and Thompson [40]. Since the absolute velocities of the two fronts must be equal (for steady-state growth), it is advantageous to plot the absolute velocities of the crystal and amorphous growth regimes on the same plot. For "back-side" growth, the amorphous melting line crosses the growth curve before the maximum velocity is attained, allowing the maximum EC velocity to equal the maximum crystal growth velocity. For "front-side" growth, the amorphous melting line crosses the growth curve after the maximum in the IRF for the crystal growth; thus, a tie-line connecting the maximum growth velocity with the corresponding melting velocity predicts a temperature gradient where the amorphous front has a higher temperature. This prevents the required heat transfer from the crystal front across the liquid layer to the amorphous front which drives the process. This has the result that the maximum EC velocity is limited to the point where the two curves cross. It is also to be noted that the maximum predicted velocity in the case of "front-side" growth corresponds to a liquid layer of zero width which should arrest the moving fronts since instabilities or fluctuations at the interface could easily quench the mediating liquid—leaving only the far slower process of solid-phase epitaxy to effect crystallization. For these reasons, IRFs play a key role in understanding EC.

The simulation data drawn in Fig. 9 allows a determination of whether front-side vs. back-side growth is suggested for Si. The raw data for the IRFs suggest that "back-side" growth is more likely to occur; with the caveat that, since the amorphous melting curve essentially starts 130K lower than it should if it were to reproduce the experimental melting point, this result is almost guaranteed. We believe that it is more instructive to look at the point of intersection of "shifted" data for the amorphous melting curve (shifted so that the experimental melting point is reproduced) and the crystalline freezing curve. These lines cross at a point too close to the crystal solidification peak to make a conclusive determination of front-side vs. back-side growth for Si (especially considering the scatter in the amorphous melting data, as mentioned above). While the simulation results are ambiguous regarding the type of growth, experimental results suggest that the maximum crystalline regrowth velocity and the maximum EC are both near 15 m/s [1,2,9–11,38]. If these values are indeed the same, then "front-side" growth must be ruled out due to a vanishing mediating liquid layer. Thus, we believe "back-side" growth is more likely (reinforced by our results for Ge which indicates that EC exhibits "back-side" growth [41]).

It can be seen from Fig. 10 that there are two interface temperatures which correspond to a given velocity of the amorphous interface under conditions of backside growth. The lower temperature can be designated as the "unstable growth temperature" because temperature fluctuations in either direction will result in the interface velocity fluctuations in the same direction encouraging further temperature fluctuation until the interface velocity is either at zero or at the maximum. The higher temperature is considered the "stable growth temperature" because fluctuations in temperature are met by counter-fluctuations in velocity and so the temperature will tend to stabilize. For high enough substrate temperatures, steady-state EC can occur with crystal growth corresponding to the stable portion of the IRF curve. When the substrate temperature is lower, interface temperatures are driven down which is most easily satisfied by crystal growth occurring on the unstable side of the IRF. Since the temperature of the substrate is still below that of both interfaces, the interfaces will tend to undergo variations toward lower temperature causing the crystal velocity to reduce further and the process to propagate (corresponding to the arrows labeled I and IV in Fig. 11). Eventually, the crystal interface will be at a lower temperature than the amorphous interface causing the heat transfer direction to reverse and the crystal interface to heat up (arrows II and III in Fig. 11). This will continue until the interface velocity reaches its maximum (when it is effectively stable again). The process will then repeat itself which could result in the "scalloped" morphology observed after EC of germanium by Chojnacka and Thompson [39] (it is generally accepted that Si and Ge should behave similarly as a result of EC). This "scalloped" morphology is observed under low substrate temperatures (high heat loss) and consists of large crystalline grains around 0.5 μm in size interspersed

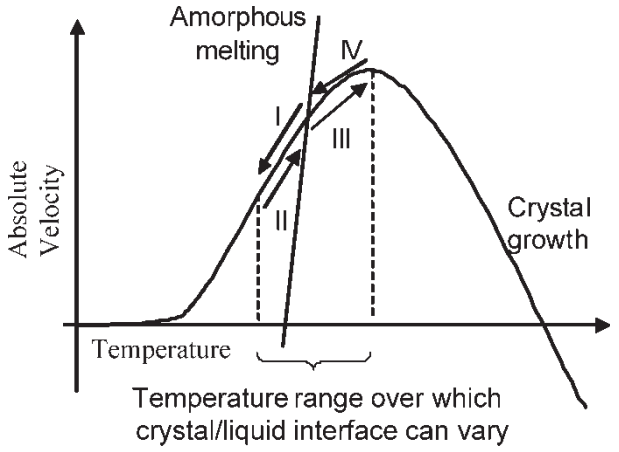

FIGURE 11 Demonstration of "stable", back-side, explosive crystallization on the unstable side of the IRF. Regions I through IV are explained within the text. Dashed vertical lines define the temperature range over which the crystal/liquid interface can vary.

with very fine grained, or even amorphous, sections of similar lengthscale oriented parallel to the growth front. According to the explanation above, at any given instant, the crystal/melt interface is capable of fluctuations in velocity such that its range may encompass values faster or slower than that of the nearby amorphous/melt interface. (Since the amorphous melting line is considered stable, we will assume that its speed is relatively constant). The result would be manifested as a change in liquid layer width. When the liquid layer is very thin (say, 1 atomic layer, or 2.8 Å), there may not be enough mobile atoms to sustain large-grain growth, resulting in the less ordered (fine-grained or amorphous) structure.

A second possible explanation of the scalloped morphology can be taken from the experimental observation that liquid silicon solidifying at rates above 15 m/s [13,38] forms an amorphous phase. Assuming Ge also possesses a limiting amorphization velocity above which solidification to produce amorphous material is the only possible outcome, solid growth can occur at rates higher than this critical velocity near the peak of the IRF, explaining why some of the growth results in fine-grained crystalline or amorphous germanium. These possible explanations for the observation of differing growth morphologies are based on the assumption of "backside" growth, which this paper (complemented by the results in Ref. [41]) has concluded is the preferred mode of growth for an enhanced SW model for germanium. For Si, the picture is less clear since the results obtained here are not unambiguously backside growth, as discussed above.

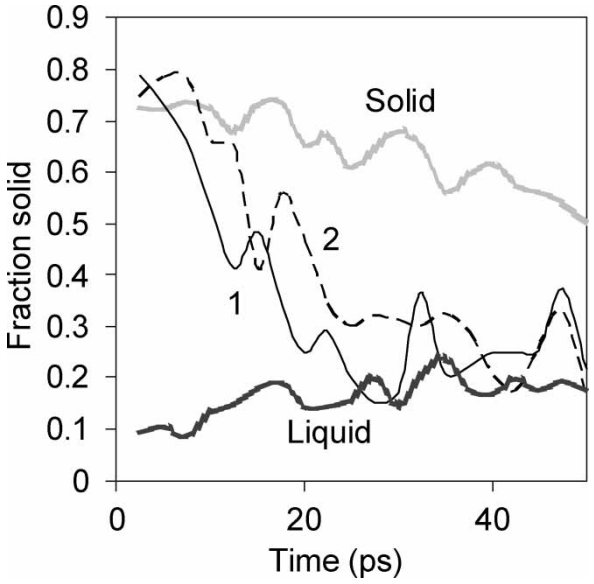

FIGURE 12 Time evolution of the order within various slices of the system. The numbered lines refer to slices which were originally amorphous but which were melted in the wake of the moving solid–liquid interface. The labels "solid" and "liquid" refer to slices which did not experience the passage of the interface. The *y*-axis represents the fraction of solid atoms in a given slice.

MECHANISM FOR MELTING AMORPHOUS Si

Unlike the case for melting at a crystal-melt interface, we found that *a*-Si does not melt exclusively at the moving planar interface. Figure 12 shows a characteristic plot of the slice-by-slice analysis that we undertook to determine the location of the interface during melting for the SW115 potential at a temperature of 1450K (c.f. T_m for this potential model is 1325K). Plots for other temperatures and potential models are qualitatively similar and are omitted for brevity. As time progresses, all the amorphous slices that did not experience the passage of the melt front (labeled as "solid" in Fig. 12) "soften" toward the liquid phase (i.e. they lose order). Interfacial melting is also present, as can be observed in Fig. 12 when the order in a slice drops quickly (for example, slice 2 at around 10 ps) as the melt front sweeps through the slice. The general trend for a given slice is to continuously disorder toward a liquid-like order in anticipation of the arrival of the solid–liquid interface which converts the entire slice to liquid. So, while interfacial melting does occur, homogeneous melting occurs concurrently, giving rise to a softening of the amorphous solid. Three different potential formalisms (EDIP, MEAM and SW) as well as three parameterizations of the SW potential gave qualitatively similar results implying that the softening we observed is not an artifact of the potential model or the reparameterization presented in this paper. Thus *a*-Si melts at both at the interface and via homogeneous melting.

Aside from the data shown in Fig. 12, several other results corroborate our statement above regarding the amorphous melting mechanism. First, there is no noticeable superheating of the amorphous samples when melted from the bulk. Figure 13 shows volume–temperature plots for the original SW, SW115, and EDIP potentials. The volume change upon melting (a decrease for silicon which would be a step-change for a first-order transition) provides a way to determine the melting temperature for these samples, influenced by superheating due to the absence of an interface or surface. Equilibrated 1000-atom samples with periodic boundary conditions in all three directions were evolved at constant temperature and pressure to produce the results shown in Fig. 13. The predicted melting points (or melting point range) for all three potentials (1100K for SW, 1100–1200K for EDIP, and 1275–1375K for SW115) show no noticeable superheating compared to the values obtained from the IRF.

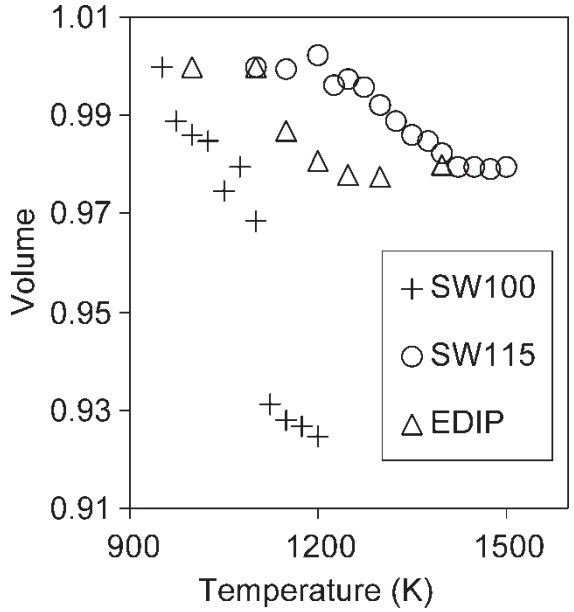

FIGURE 13 Volumetric plot to determine the melting point. The volume is normalized by its value at the lowest temperature reported. Key as given in the inset.

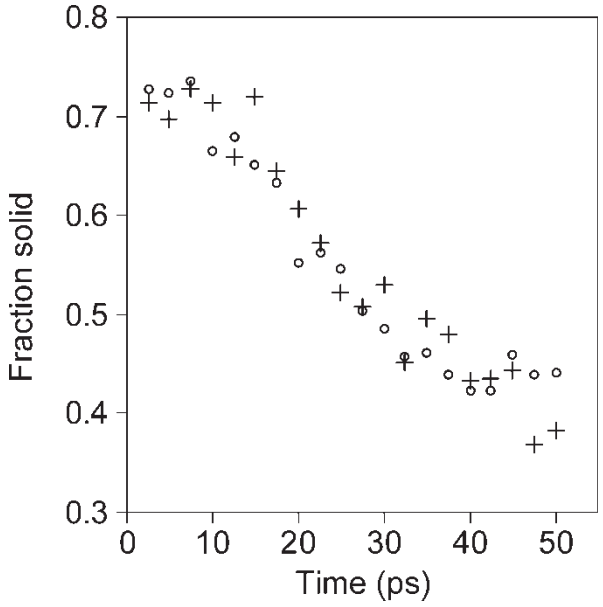

FIGURE 14 Comparison of bulk melting in a system without an interface (+symbols) to melting of "bulk-like slices" (open circles) taken from the evolution of the interfacial sandwich configuration. The y-axis represents the fraction of solid atoms in the sample. The temperature in both cases is 1400K.

The absence of superheating raises the probability for homogeneous melting to occur in the bulk amorphous region physically removed from the liquid-amorphous interface. Neither the EDIP nor the SW115 potential models show a first-order amorphous melting transition, in contrast to the original SW potential and earlier results [42–45] but, since all the parameterizations of the SW potential exhibit homogeneous melting, it is clear that this presumed deficiency in the SW115 and EDIP models has little impact on the mode of amorphous melting. The SW115 model exhibits a first-order transition when the crystal melts, a crucial requirement for any acceptable model.

A second confirmation of the presence of homogeneous melting is seen in Fig. 14 which compares the slices identified by the order parameter as constituting unequivocally "bulk" amorphous material in the interfacial system with truly bulk samples having the same number of atoms and aspect ratio as the sandwich samples and evolved under the same conditions. The rate of melting is similar in both cases, indicating that the bulk-like slices in the simulations used to determine the IRF are, indeed, melting homogeneously.

To ensure that the melting mechanism is not an artifact of the selected order parameter, a second order parameter, with an entirely different genesis [46], was used to analyze the system. Implementation of this alternate order parameter also predicted the same melting mechanism. Figure 15 shows three snapshots (at 5, 30 and 50 ps) of half of a sandwich configuration of *a*-/*l*-/*a*-Si evolved at 1450K analyzed using the order parameter given in Eq. (2) as well as a snapshot of the same system at 50 ps evaluated using the order parameter devised by Shetty *et al.* [46]. These snapshots provide a visual appreciation for the melting mechanism, and illustrate the diffuseness of the planar solid/liquid interface. Clearly then, homogeneous melting of the bulk is actively accompanying heterogeneous melting at the planar solid–liquid interface.

The data shown in Figs. 12 and 15 reveal that the thickness of the amorphous-liquid interface is several atomic layers wide. A given slice takes about 10 ps to fully convert from *a*-Si to liquid. Knowing the interface velocity, we can estimate the interface thickness to be ≈ 1 nm on average (about 4 atomic layers). This is significantly wider than that of a comparable crystal/liquid interface (1–2 atomic layers), but it is not unexpected given the similarity in structure between the two phases. However, the slice-by-slice analysis used in the results above is not well suited to examine in detail the roughness of the interface. To address this concern, the samples were analyzed using the signature cell order parameter due to Shetty *et al.* [46]. The results (of which Fig. 16 is a characteristic example) show that the diffuse interface is indeed rough. Snapshots of the time evolution of the system (not shown) demonstrated that the shape of the interface is not coherent as a function of time, changing its shape in a stochastic manner. As a result, we attribute the roughness of the interface to stochastic differences in the local melting rate.

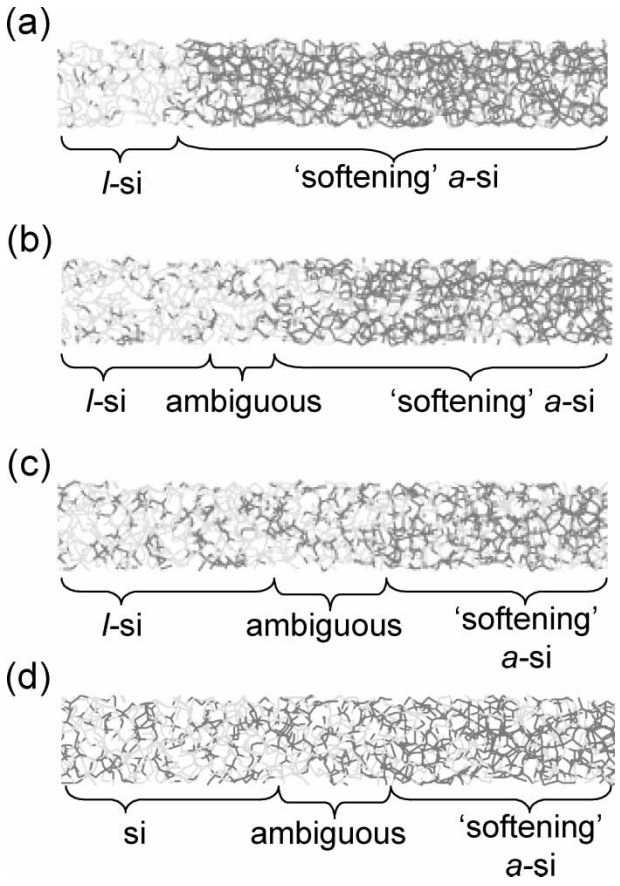

FIGURE 15 Snapshots illustrating the time evolution of an amorphous-liquid-amorphous system at (a) 5 ps, (b) 30 ps, and (c) 50 ps evolved at 1450K. Only half of the simulation cell is shown for clarity. The softening of the *a*-Si section can be seen by the draining of color in the amorphous region as time progresses. From these snapshots, it is hard to visualize the ambiguous region connecting liquid and amorphous regions and its extent was determined by an analysis of the order parameter. There is no ambiguously ordered section in the system after 5 ps. Snapshot (d) shows the same system as that in (c) but analyzed using the signature cell [44] order parameter instead of the angular order parameter [30] used throughout the paper.

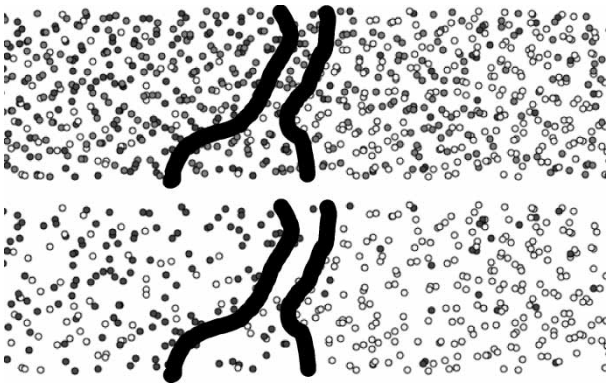

FIGURE 16 Snapshot of one of the amorphous-liquid interfaces taken from an amorphous-liquid-amorphous system (i.e. snapshot represents half of the box) evolved at 1450K (above the melting point for amorphous silicon for this potential). The order of an individual atom was determined using the signature cell order parameter [44] in which darker atoms are more ordered. The top figure represents all of the atoms in this region of the sample; the bottom figure represents only those atoms which are particularly high or low in order to make clearer an observation of the location and shape of the interface. The thick black lines split the sample into unambiguously amorphous (left), unambiguously liquid (right), and ambiguously ordered material (between the black lines). The roughness of the interface is clearly visible. The extent of the interface in this snapshot ranges from 4–19 Å thick.

CONCLUSIONS

This paper has presented a new parameterization of the SW potential tailored to fit all three condensed phases of silicon as much as possible. This parameterization was used to determine the IRFs for both the crystal and amorphous phases of silicon and demonstrated superior performance over IRFs created with other potentials including two other parameterizations of the SW potential, and the original parameterizations of the SW, EDIP and MEAM potentials.

From the IRF data, it could not be conclusively determined that Si exhibits "back-side" growth, but the suggestion that the modulus of the *a*-Si melting line is close to the maximum of the crystalline IRF is intriguing, given that our results for similarly modified SW models for Ge more clearly demonstrate back-side growth [41]. These computational results for Ge and Si suggest that Ge might more readily undergo EC than Si and this is, indeed, observed experimentally. The results also show that the interplay between the kinetics of growth of crystal and amorphous phases is intimately involved in EC. The point at which the amorphous melting curve and the crystal freezing curve cross determines much about EC and probably has a direct impact on whether the process is possible for a given material.

The melting of amorphous silicon is more complex than the single mode heterogeneous melting observed at planar crystal-melt interfaces. Our results show that, while melting of the amorphous phase does occur at the moving interface, this is accompanied by homogeneous melting within the amorphous solid itself. We suggest that the appearance of homogeneous melting is enabled by the inability of the amorphous material to superheat to any great extent and the smaller difference in order than a comparable crystal-melt system. Given this complication, the use of IRFs to represent the melting of amorphous materials may be less appropriate than has previously been realized.

Acknowledgements

The authors would like to thank Professor Michael O. Thompson and Dr Aleksandra Chojnacka for thier help in interpreting the simulation results in the light of their EC experiments and Professor Michael O. Thompson for reading this manuscript. The authors would also like to thank the National Science

Foundation for funding this research through a KDI award (9980100) and the Cornell Center for Materials Research for providing much of the computational resources necessary for this computationally intensive study.

References

[1] Thompson, M.O., Galvin, G.J., Mayer, J.W., Peercy, P.S., Poate, J.M., Jacobson, D.C., Cullis, A.G. and Chew, N.G. (1984) "Melting temperature and explosive crystallization of amorphous silicon during pulsed laser irradiation", *Phys. Rev. Lett.* **52**, 2360.

[2] Donovan, E.P., Spaepen, F., Turnbull, D., Poate, J.M. and Jacobson, D.C. (1983) "Heat of crystallization and melting point of amorphous silicon", *Appl. Phys. Lett.* **42**, 698.

[3] Gore, G. (1855) "On a peculiar phenomenon in the electrodeposition of antimony", *Philos. Mag.* **9**, 73.

[4] Coffin, C.C. and Johnston, S. (1934) "Studies of explosive antimony I—the microscopy of polished surfaces", *Proc. R. Soc. A* **146**, 564.

[5] Kuz'menko, V.M., Mel'nikov, V.I. and Rakhubovskii, V.A. (1984) "Mechanisms of spontaneous crystallization of amorphous metallic films", *Sov. Phys. JETP* **59**, 612.

[6] Das, V.D. and Lakshmi, P.J. (1988) "Electron-beam-induced explosive crystallization of amorphous Se80Te20 alloy thin films and oriented growth of crystallites", *Phys. Rev. B* **37**, 720.

[7] Willems, G.J., Wouters, D.J. and Maes, H.E. (1993) "Explosive crystallization of amorphous Si_3N_4 films on silicon during silicon laser melting", *J. Appl. Phys.* **74**, 5196.

[8] Bensahel, D. and Auvert, G. (1983) "Explosive crystallization in *a*-Ge and *a*-Si: a review", In: Marayan, J., Brown, W.L. and Lemons, R.A., (eds) *Laser-Solid Interact. Transient Therm. Process. Mater.* (Mater. Res. Soc. Symp. Proc., New York, NY), Vol. 13, pp 165–176.

[9] Lowndes, D.H., Jellison, G.E., Jr., S, J.R., Pennycook, J., Withrow, S.P. and Mashburn, D.N. (1986) "Direct measurements of the velocity and thickness of explosively propagating buried molten layers in amorphous silicon", *Appl. Phys. Lett.* **48**, 1389.

[10] Stolk, P.A., Polman, A. and Sinke, W.C. (1993) "Experimental test of kinetic theories for heterogeneous freezing in silicon", *Phys. Rev. B* **47**, 5.

[11] Murakami, K., Eryu, O., Takita, K. and Masuda, K. (1987) "Explosive crystallization starting from an amorphous-silicon surface region during long pulsed-laser irradiation", *Phys. Rev. Lett.* **59**, 2203.

[12] Voogt, F.C. and Ishihara, R. (2001) "A combined TEM and time-resolved optical reflectivity investigation into the excimer-laser crystallization of *a*-Si films", *Thin Solid Films* **383**, 45.

[13] Galvin, G.J., Mayer, J.W. and Peercy, P.S. (1985) "Solidification kinetics of pulsed laser melted silicon based on thermodynamic considerations", *Appl. Phys. Lett.* **46**, 644.

[14] Tsao, J.Y., Peercy, P.S. and Thompson, M.O. (1987) "Interfacial overheating during melting of Si at 190 m/s", *J. Mater. Res.* **2**, 91.

[15] Larson, B.C., Tischler, J.Z. and Mills, D.M. (1986) "Nanosecond resolution time-resolved X-ray study of silicon during pulsed-laser irradiation", *J. Mater. Res.* **1**, 144.

[16] Brambilla, L., Colombo, L., Rosato, V. and Cleri, F. (2000) "Solid–liquid interface velocity and diffusivity in laser-melt amorphous silicon", *Appl. Phys. Lett.* **77**, 2337.

[17] Luedtke, W.D. and Landman, U. (1988) "Preparation and melting of amorphous silicon by molecular-dynamics simulations", *Phys. Rev. B* **37**, 4656.

[18] Luedtke, W.D. and Landman, U. (1989) "Preparation, structure, dynamics, and energetics of amorphous silicon: a molecular-dynamics study", *Phys. Rev. B* **40**, 1164.

[19] Choudhary, D. (2004) "Order-property relations in semiconducting materials", Ph.D. Thesis (Cornell University).

[20] Keblinski, P., Bazant, M.Z., Dash, R.K. and Treacy, M.M. (2002) "Thermodynamic behavior of a model covalent material described by the environment-dependent interatomic potential", *Phys. Rev. B* **66**, 064104.

[21] Kluge, M.D. and Ray, J.R. (1989) "Velocity versus temperature relation for solidification and melting of silicon: a molecular-dynamics study", *Phys. Rev. B* **39**, 1738.

[22] Yu, Q., Thompson, M.O. and Clancy, P. (1996) "Solidification kinetics in SiGe alloys", *Phys. Rev. B* **53**, 8386.

[23] Stillinger, F.H. and Weber, T.A. (1985) "Computer simulation of local order in condensed phases of silicon", *Phys. Rev. B* **31**, 5262.

[24] Bazant, M.Z. and Kaxiras, E. (1996) "Modeling of covalent bonding in solids by inversion of cohesive energy curves", *Phys. Rev. Lett.* **77**, 4370.

[25] Bazant, M.Z., Kaxiras, E. and Justo, J.F. (1997) "Environment-dependent interatomic potential for bulk silicon", *Phys. Rev. B* **56**, 8542.

[26] Justo, J.F., Bazant, M.Z., Kaxiras, E., Bulatov, V.V. and Yip, S. (1998) "Interatomic potential for silicon defects and disordered phases", *Phys. Rev. B* **58**, 2539.

[27] Lenosky, T.J., Sadigh, B., Alonso, E., Bulatov, V.V., Diaz de la Rubia, T., Kim, J., Voter, A.F. and Kress, J. (2000) "Highly optimized empirical potential model of silicon", *Model. Simul. Mater. Sci. Eng.* **8**, 825.

[28] Goedecker, S. (2002) "Optimization and parallelization of a force field for silicon using OpenMP", *Comp. Phys. Comm.* **148**, 124.

[29] Kluge, M.D., Ray, J.R. and Rahman, A. (1987) "Amorphous-silicon formation by rapid quenching: a molecular-dynamics study", *Phys. Rev. B* **36**, 4234.

[30] Barkema, G.T. and Mousseau, N. (2000) "High-quality continuous random networks", *Phys. Rev. B* **62**, 4985.

[31] Brown, D. and Clarke, J.H.R. (1984) "A comparison of constant energy, constant temperature and constant pressure ensembles in molecular dynamics simulations of atomic liquids", *Mol. Phys.* **51**, 1243.

[32] Uttormark, M.J., Thompson, M.O. and Clancy, P. (1993) "Kinetics of crystal dissolution for a Stillinger–Weber model of silicon", *Phys. Rev. B* **47**, 15717.

[33] Vink, R.L.C., Barkema, G.T., van der Weg, W.F. and Mousseau, N. (2001) "Fitting the Stillinger–Weber potential to amorphous silicon", *J. Non-Cryst. Solids* **282**, 248.

[34] Baeri, P., Foti, G., Poate, J.M. and Cullis, A.G. (1980) "Phase transitions in amorphous Si produced by rapid heating", *Phys. Rev. Lett.* **45**, 2036.

[35] Fortner, J. and Lannin, J.S. (1989) "Radial distribution functions of amorphous silicon", *Phys. Rev. B* **39**, 5527.

[36] Laaziri, K., Kycia, S., Roorda, S., Chicoine, M., Robertson, J.L., Wang, J. and Moss, S.C. (1999) "High resolution radial distribution function of pure amorphous silicon", *Phys. Rev. Lett.* **82**, 3460.

[37] Bucksbaum, P.H. and Bokor, J. (1984) "Rapid melting and regrowth velocities in silicon heated by ultraviolet picosecond laser pulses", *Phys. Rev. Lett.* **53**, 182.

[38] Thompson, M.O., Mayer, J.W., Cullis, A.G., Webber, H.C., Chew, N.G., Poate, J.M. and Jacobson, D.C. (1983) "Silicon melt, regrowth, and amorphization velocities during pulsed laser irradiation", *Phys. Rev. Lett.* **50**, 896.

[39] Chojnacka, A. and Thompson, M.O. (2001) "Morphological instabilities during explosive crystallization of germanium films", In: Moss, S.C., Poker, D.B. and Ila, D., eds, *Growth, Evolution and Properties of Surfaces, Thin Films and Self-Organized Structures* (Mat. Res. Soc. Symp. Proc., Warrendale, PA), Vol. 648, pp P11.12.1–P11.12.8.

[40] Chojnacka, A. (2002) "Explosive crystallization of germanium films: kinetics and morphologies", Ph.D. Thesis (Cornell University).

[41] Albenze, E.J., Matejik, L.A., Fynan, N.F. and Clancy, P. (2003) "Prediction of the interface response functions for amorphous and crystalline phases of silicon and germanium", In: Abelson, J.R., Ganguly, G., Matsumura, H., Robertson, J. and Schiff, E.A., eds, *Amorphous and Nanocrystalline Silicon-Based Films—2003* (Mat. Res. Soc. Symp. Proc., Warrendale, PA), Vol. 762, pp A16.4.1–A16.4.6.

[42] Rosato, V. and Celino, M. (1999) "Tight binding simulation of the thermodynamic behavior of amorphous silicon", *J. Appl. Phys.* **86**, 6826.

[43] Campisano, S.U., Jacobson, D.C., Poate, J.M., Cullis, A.G. and Chew, N.G. (1985) "Si liquid-amorphous transition and impurity segregation", *Appl. Phys. Lett.* **46**, 846.
[44] Campisano, S.U., Jacobson, D.C., Poate, J.M., Cullis, A.G. and Chew, N.G. (1984) "Impurity and interfacial effects on the formation of amorphous Si from the melt", *Appl. Phys. Lett.* **45**, 1216.
[45] Cullis, A.G., Webber, H.C. and Chew, N.G. (1982) "Ultrarapid crystal growth and impurity segregation in amorphous silicon annealed with short Q-switched laser pulses", *Appl. Phys. Lett.* **40**, 998.
[46] Shetty, R., Choudhary, D., Clancy, P. and Escobedo, F. (2002) "A novel algorithm for characterization of order in materials", *J. Chem. Phys.* **117**, 4000.